Journal of Power Sources 466 (2020) 228283

Contents lists available at ScienceDirect

Journal of Power Sources

journal homepage: www.elsevier.com/locate/jpowsour

Perspective

First results from *in situ* transmission electron microscopy studies of all-solid-state fluoride ion batteries

Mohammed Hammad Fawey [a,b,c,*], Venkata Sai Kiran Chakravadhanula [d,e,**], Anji Reddy Munnangi [d], Carine Rongeat [d], Horst Hahn [b,c,d], Maximilian Fichtner [b,d], Christian Kübel [b,c,d,f]

[a] Physics Department, Faculty of Science, Sohag University, 82524, Sohag, Egypt
[b] Institute of Nanotechnology (INT), Karlsruhe Institute of Technology (KIT), Hermann-von-Helmholtz-Platz 1, 76344, Eggenstein-Leopoldshafen, Germany
[c] Joint Research Laboratory Nanomaterials, Technical University Darmstadt, Alarich-Weiss-Straße 2, 64287 Darmstadt, Germany
[d] Helmholtz Institute Ulm for Electrochemical Energy Storage (HIU), Albert-Einstein-Allee 11, 89081, Ulm, Germany
[e] Vikram Sarabhai Space Center, Kerala, 695022, India
[f] Karlsruhe Nano Micro Facility (KNMF), Karlsruhe Institute of Technology, Hermann-von-Helmholtz-Platz 1, 76344, Eggenstein-Leopoldshafen, Germany

HIGHLIGHTS

- CV peaks measured during the *in situ* TEM and *ex situ* studies are comparable.
- The expected formation of CuF_2 was confirmed at the cathode-electrolyte interface.
- Cu grain growth, Cu diffusion into electrolyte and void formation were observed.
- Capacity fading could be explained by copper oxide formation as a side reaction.

GRAPHICAL ABSTRACT

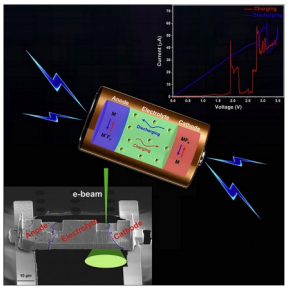

ARTICLE INFO

Keywords:
In situ transmission electron microscopy (TEM)
Focused ion beam (FIB)
Fluoride ion battery
All-solid-state battery
Electrode/electrolyte interfaces
Electrochemistry

ABSTRACT

A focused ion beam (FIB) system is used to fabricate a micron-sized all-solid-state fluoride ion cell from a bulk battery for *in situ* transmission electron microscopy (TEM) testing. The bulk battery is based on a $La_{0.9}Ba_{0.1}F_{2.9}$ solid-state electrolyte with a nanocomposite of Cu/C as a cathode and a nanocomposite of MgF_2, Mg, $La_{0.9}Ba_{0.1}F_{2.9}$ and C as an anode. The evolution of the morphology, structure, and composition of the electrodes and their interfaces with the electrolyte is characterized using *in-situ* TEM during electrochemical cycling. The high-resolution transmission electron microscopy (HRTEM) and scanning transmission electron microscopy-energy dispersive X-ray (STEM-EDX) analysis of the cathode-electrolyte interface reveal the expected formation of CuF_2 phase during charging. During cycling, grain growth of Cu in the cathode ingredients and Cu diffusion from the cathode into the electrolyte are observed in addition to void formation.

* Corresponding author. Physics Department, Faculty of Science, Sohag University, 82524, Sohag, Egypt.
** Corresponding author. Vikram Sarabhai Space Centre (VSSC), Indian Space Research Organisation (ISRO), Thiruvananthapuram, Kerala, 695022, India.
E-mail addresses: mohammed.fawey@gmail.com (M.H. Fawey), cvs_kiran@vssc.gov.in (V.S.K. Chakravadhanula), christian.kuebel@kit.edu (C. Kübel).

https://doi.org/10.1016/j.jpowsour.2020.228283
Received 15 February 2020; Received in revised form 15 April 2020; Accepted 28 April 2020
Available online 19 May 2020

1. Introduction

Over the last decades, great efforts have been exerted to develop efficient approaches to produce energy from renewable sources and to develop suitable energy storage systems. Rechargeable batteries are currently one of the most promising energy storage systems. They are investigated for a wide variety of applications such as electric vehicles (EV) and hybrid electric vehicles (HEV) [1,2], uninterrupted power supply (UPS) systems [3], grid stabilization [2], portable and soft electronics [4,5], and spacecraft [6]. So far, the main focus has been on lithium-ion batteries (LIBs) because of their high gravimetric and volumetric energy densities [7,8]. However, the application of LIBs is limited because of their environmental requirements, safety risks, and the high cost. Moreover, lithium could be in short supply in the near future based on optimistic EV/HEV production scenarios and the low availability of lithium sources [9]. Besides, some applications like EV require longer battery lifetimes and higher power and energy density than offered by present LIBs [10,11]. Therefore, huge efforts are currently exerted to find alternative batteries to reach the required energy density and application properties. Apart from this, alternative battery technologies based on anions or cation chemistries such as Cl^- [12,13], F^- [14–18], Mg^+ [19,20] and Na^+ [21–23] have been investigated. Fluoride ion batteries appear as one promising candidate as they offer high theoretical energy densities of more than 5000 $Wh.L^{-1}$, (50% above the theoretical capacity of the Li-air cell) [24]. Moreover, fluorine has a high natural abundance, hence, comparably low cost. Recently, the principle of a secondary battery based on a fluoride ion shuttle has been demonstrated [14]. However, fluoride ion batteries are currently limited to operate at elevated temperatures of 150 °C and above as the electrolytes have high ionic conductivity only at high temperatures [17,25,26]. Currently, fluoride ion batteries are at an early stage of development and large improvements are needed to meet the requirements for reliable long-term operation. Normally, understanding the fundamental behavior of the materials during the electrochemical reaction is essential to optimize different performance aspects such as energy density, power density, elevated operating temperature, safety, cycle life, and self-discharge rate. For this purpose, the characterization of a battery at various stages i.e., before, during, and after cycling is critical. Although *ex situ* characterization of battery materials is an important step to understand their structure and reaction products, it only allows characterizing specific individual states of various samples. Therefore, *ex situ* studies leave many open questions about kinetics, ion-interaction and cell-degradation mechanisms, in addition to relaxation processes during transfer and analysis affecting the observed structure [27]. In contrast, real-time observation of phase transformations, morphological, structural and compositional variations during electrochemical cycling becomes indispensable to identify the intermediate metastable phases and understand the side reactions. Currently, major attempts are made to perform *in situ* studies using characterization techniques at various length scales, (e.g. optical microscopy [28,29], scanning electron microscopy (SEM) [30,31], TEM [32,33], X-ray diffraction [34,35], neutron diffraction [36,37], and Raman spectroscopy [38,39]). Among these techniques, TEM is the only characterization tool that provides direct structural, compositional and morphological information up to atomic resolution. As the materials used in fluoride ion batteries are generally stable under the electron beam, all-solid-state rechargeable fluoride ion batteries are a good model system for *in situ* electrochemical studies inside the TEM. In the present work, a $Cu/La_{0.9}Ba_{0.1}F_{2.9}/MgF_2$ full cell has been investigated by *in situ* TEM electrochemical cycling to study the underlying processes providing a detailed understanding of the variations of the morphology, structure, and composition at the interfaces. Here, an optimized FIB preparation technique [15] has been employed to prepare micron-sized cells from the all-solid-state bulk fluoride ion battery.

2. Experimental procedures

2.1. Materials synthesis

The bulk battery was prepared using a composite of Mg, MgF_2, C, and $La_{0.9}Ba_{0.1}F_{2.9}$ as an anode, a composite of Cu and C as a cathode and $La_{0.9}Ba_{0.1}F_{2.9}$ as a solid electrolyte. The cathode and anode composites were prepared by ball-milling of the corresponding compounds [26], while the tysonite-type $La_{0.9}Ba_{0.1}F_{2.9}$ electrolyte was prepared by ball-milling of LaF_3 and BaF_2 [14]. The weight ratio of the anode material was 20% Mg, 20% MgF_2, 10% carbon black, and 50% $La_{0.9}Ba_{0.1}F_{2.9}$. The weight ratio of the cathode material was 90% Cu and 10% carbon black. Cu has been chosen as cathode material because of the high theoretical capacity of the Cu/CuF_2 couple (528 mAh g^{-1} [40]) and the high potential vs. Mg/MgF_2 (2.71 V). Mg metal is sensitive to surface oxidation, even when stored under Ar, hence, rapid performance degradation occurs when used as anode [26]. However, the poor reactivity and the low ionic conductivity of MgF_2 prevents its direct use as an anode. Therefore, a mixture of Mg and MgF_2 was used to enhance the reactivity [26,41]. Moreover, adding the electrolyte and carbon to the electrode was necessary to ensure both ionic and electronic conductivity as the pure metal fluorides are insulators and poor ionic conductors.

2.2. FIB fabrication of micron-sized battery systems

The initial all-solid-state battery was assembled by compacting the powders of the anode, electrolyte, and cathode in layers forming a pellet of 7 mm diameter (Fig. S1 a, Supplementary Data). To enable FIB cross-section preparation across the anode/electrolyte/cathode within one TEM lamella, the starting battery pellet was repressed at 5 GPa using 8 mm dies to reduce the electrolyte thickness to around 20–30 μm and to reduce the porosity thus strengthening the lamella mechanically (Fig. S1 b, Supplementary Data). Enabling a nearly uniform electrolyte thickness throughout the pellet is challenging but it can be achieved by careful distribution of the starting powder layers. As detailed in Ref. [15], a FIB (FEI Strata 400S) was used to mill a micron-sized cell of approximately $70 \times 35 \times 8$ μm^3 from the bulk battery (Fig. S2 a, Supplementary Data). Hence, the areas of interest around the electrode-electrolyte interfaces were thinned to electron transparency (Fig. S2 b, Supplementary Data). An Omniprobe 200 micromanipulator was used to place the micron-sized cell on a MEMS-based electro-contacting device (Protochips Inc.). Finally, the micron-sized cell was contacted using local Pt-deposition between the electrical contacts of the MEMS device and the anode/cathode to enable the electrochemical biasing.

2.3. Electrochemical measurements

Before carrying out the *in situ* TEM studies, a bulk sample of the same battery system ($Cu//La_{0.9}Ba_{0.1}F_{2.9}//Mg + MgF_2$) has been cycled *ex situ* by applying a current density of ±4 mA□g^{-1} at an elevated temperature of 150 °C, where the capacity evolution upon 20 cycles has been obtained [26]. Moreover, in the present work, a micron-sized $Cu/LaBaF/MgF_2$ full cell was cycled *ex situ* in a high vacuum of approximately 10^{-7} mbar at room temperature (RT). The cell was charged by applying a voltage sweep from 0 to 3.5 V over 4 h. Subsequently, discharging was performed by sweeping the voltage from 3.5 V to 0 V over 4 h.

For *in situ* studies, another micron-sized $Cu/LaBaF/MgF_2$ full cell was studied *in situ* inside a Titan 80–300 TEM (FEI Company) using an Aduro single tilt sample holder (Protochips Inc.) and a Keithley 2611A source meter. The electrochemical measurements were performed by cyclic voltammetry (CV) at RT. The micron-sized full cell was charged by applying a voltage sweep from 0 V to 3.5 V over 2 h. Then, the voltage was held at 3.5 V for 30 min to enable TEM investigation. Afterward, discharging was performed by sweeping the voltage from 3.5 V to 0 V over 2 h. Using the same conditions, a second cycle was started.

3. Results & discussion

3.1. Electron beam effects on the micron-sized battery

The electron microscopic imaging and spectroscopy provide significant information about the chemical composition and micro/nano-structure of materials with high spatial resolution. However, the electron beam of the electron microscope may also cause undesirable changes in the surface or the bulk structure of the specimen under investigation. Therefore, before preparing the sample for the *in situ* TEM studies, the as-prepared components of the fluoride ion battery were investigated to study the electron beam effect on the materials. The results confirmed that the fluoride ion battery materials are stable under the normal operation conditions, so that standard TEM techniques can be used for imaging and analytical TEM of the fluoride ion battery components.

Besides, the effect of the electron beam current on the measured current in the electrochemical circuit was measured by positioning the electron beam in the TEM on the electron transparent thinned areas, the thick areas, and the Pt contacts. For these measurements, a DC voltage between 0 and 180 mV was applied to the micron-sized battery and the corresponding areas illuminated by an electron beam with a current of 9.16 nA. The thickness of the thin and thick areas was approximately 100 nm and 6 μm, respectively, while the thickness of the Pt contacts was around 4 μm. The measured current of the electron beam adding to the charging was approximately 0.5 nA, 1–2 nA and 1–1.5 nA on the electron transparent area, the thick area and the Pt contacts, respectively. These currents are negligible compared to the operating currents of the fluoride ion battery.

All of the above indicates that the all-solid-state fluoride battery is a suitable system for the *in situ* TEM electrochemical measurements.

3.2. Electrochemical study

The cell voltage vs. current for the *ex situ* charging and discharging of the micron-sized full cell is shown in Fig. 1. During the voltage sweep, the current slowly increased until it reached a first maximum around 2 V. This peak can be attributed to the formation of copper (I) oxide [26], probably due to residual oxygen present in the electrolyte and electrodes from the bulk sample preparation and/or the carbon black added to the cathode composite. A second maximum starting from around 2.77 V and continuing to 3.2 V was observed, which can be attributed to the formation of copper (II) fluoride. That potential is slightly higher than the theoretical potential of 2.71 V for the Cu/CuF_2 redox couple vs. Mg/MgF_2, which can be attributed to the polarization and, potentially, due to the small number of grains, each with different diffusion/reaction rates depending on the grain and boundary orientation. During discharging, the reverse reaction, the formation of copper (0) from the copper (II) fluoride, was observed. In addition, during charging at around 3 V a slight short circuit developed adding an ohmic behavior to the cyclic voltammetry, which is visible by the increased baseline conductivity between 3.2 and 3.5 V during charging and discharging. At 2.85 V during discharging, the short circuit increased and the I–V curve only shows an ohmic behavior. The Cu_2O formation is irreversible so that no counterpart to the oxide formation at around 2 V is observed during discharging [26]. Considering the area of the CV measurement corresponding to the Cu/CuF_2 formation, the reaction is fairly complete, based on the measured conversion charge.

Fig. 2 shows the cell voltage vs. current for the 1st *in situ* charging/discharging and the 2nd charging of the micron-sized full cell. The basic redox steps observed during charging are comparable to the *ex situ* investigation of the micron-sized full cell mentioned above. Similar potentials were also observed *ex situ* for the corresponding $Cu/La_{0.9}Ba_{0.1}F_{2.9}/CeF_3$ full battery system [26]. The electrochemical potential of Mg^{2+} and Ce^{3+} is very similar, −2.372 V and −2.336 V respectively. This confirms that the *in situ* analysis of the fluoride ion batteries yields comparable results to the *ex situ* analysis, providing a chance to study the fundamental processes in detail *in situ*. However, unfortunately, this time the charging curve is on top of strong leakage current due to a short circuit between cathode and anode, probably due to higher residual contamination during FIB preparation compared to the cell studied *ex situ*. Nevertheless, the two peaks in the charging curve indicate that the electrochemical reaction is still occurring. During the holding period at 3.5 V, the current initially slightly decreased and then suddenly jumped from ~33 μA to ~100 μA indicating a stronger short circuit formed in the cell, which may be due to Pt migration from the contacts [42]. Therefore, a strong self-discharge has to be expected during the further cycling of the cell. During discharging, the current is dominated by a short circuit, but a slight peak around 2.7 V can be seen, indicating some electrochemically driven discharging of the cell. During the 2nd charging, no characteristic CV peaks could be observed, but the micron-sized cell fractured at the cathode-electrolyte interface at a

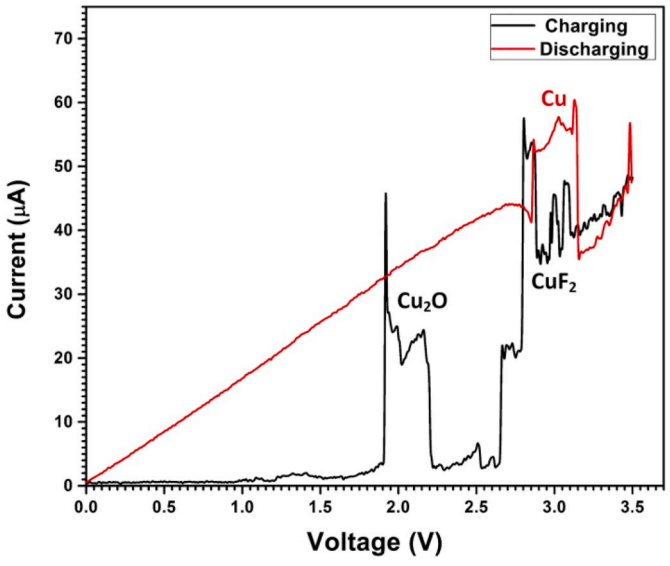

Fig. 1. *Ex situ* cyclic voltammetry (CV) curves for a thinned micron sized $Cu/LaBaF/MgF_2$ full cell.

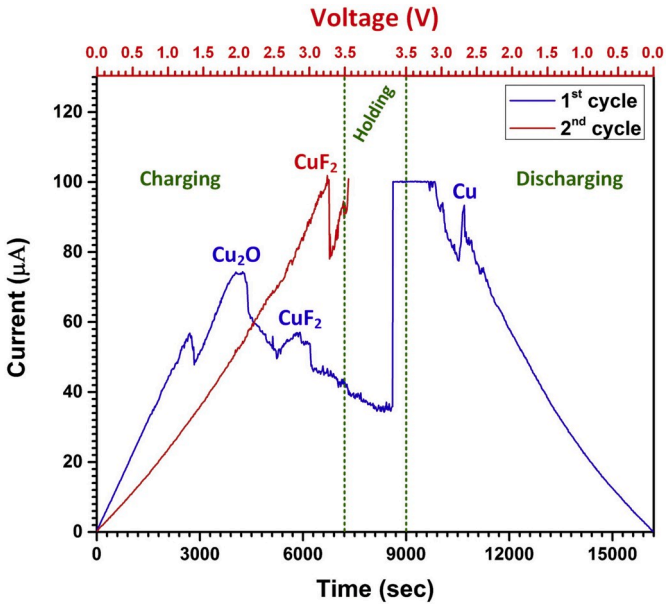

Fig. 2. Current plotted vs. voltage and time for the 1st and 2nd cycles of $Cu/LaBaF/MgF_2$ full cell.

voltage where the electrochemical reaction occurs. If this is due to the short circuit or due to limited reversibility is unclear. However, in the *ex situ* studies of the bulk battery, the capacity faded very strongly from 390 mAh g^{-1} to only 33 mAh g^{-1} after the 1st discharge [26], suggesting that only a very limited reaction should be overserved during the 2nd charging. Nevertheless, the fracture around 3.1–3.5 V suggests that some electrochemical reactions still occurred, presumably causing the fracture because of the volumetric expansion of Cu during fluorination.

3.3. STEM and SEM analysis

STEM images of the cathode-electrolyte interface before cycling, after the 1st cycle, and after a failure during the 2nd cycle are shown in Fig. 3. From the STEM images, one can see that the Cu/C cathode contains nanocrystalline Cu surrounded by carbon black. The Cu crystallite size is in the range of 40–250 nm. Comparing the STEM images of the cathode before and after the 1st cycle reveals some coarsening of the Cu. Also, void formation in the cathode is visible, to some extent after the 1st cycle and more pronounced after failure. CuF_2 formation was confirmed by HRTEM (Fig. 7), providing direct proof that the electrochemical reaction occurred despite the short circuits. Finally, a new phase can be seen as a bright line at the interface, identified from the EDS data as Mo enrichment at the interface. This Mo contamination can be attributed to the usage of the Mo TEM grid during FIB sample preparation. In contrast, on the anode side, no significant changes were observed in the thin area of the anode-electrolyte interface (Fig. S3, Supplementary Data).

The morphological changes are more pronounced at the thick part of the cathode (Fig. 4c,f). The new phase at the interface is more clearly visible compared to the thin area. Moreover, the new phase and the Cu particles are slightly protruding from the cathode due to the local volume change during charging. The volumetric change in the cathode due to the fluorination of Cu forming CuF_2 [26] is also leading to the fracture at the interface to the electrolyte (Fig. 4f). The fracture is particularly noticeable in these *in situ* samples as the porosity was reduced compared to bulk batteries cycled *ex situ*, thus providing less free volume to compensate for the volumetric changes.

On the anode side, some volumetric changes are visible as small cracks in the $Mg/MgF_2/C$ composite and at the interface with the electrolyte (Fig. 4a, d). However, more noticeable, the surface of the cycled anode (Fig. 4d) is remarkably different from the pristine anode (Fig. 4a). After cycling, the anode surface is covered by small particles in agreement with previously reported *ex situ* results where "snowflake-like" particles were formed on the anode surface [43,44]. It was found that these particles are MgF_2 sticking out of the anode surface [43–45]. The formation of these particles on the anode surface has been suggested to be the result of the low ionic conductivity of the electrolyte, leading to preferential fluoride migration on the surface [46]. If the MgF_2 formation on the anode surface is due to fast fluoride ion migration on the surface, this would significantly impact the *in situ* TEM measurements, where the surface to volume ratio of the electron transparent regions is extreme. In addition to the 20x reduced electrode thickness compared to the bulk battery, surface migration could partially explain why it is possible to cycle the micron-sized fluoride ion cell at RT, whereas elevated temperatures are needed to increase the conductivity sufficiently for the bulk battery. However, we did not observe any MgF_2 formation on the surface of the electron transparent part of the cell (only on the thicker part), which suggests that the formation of the surface decoration requires a more complex explanation.

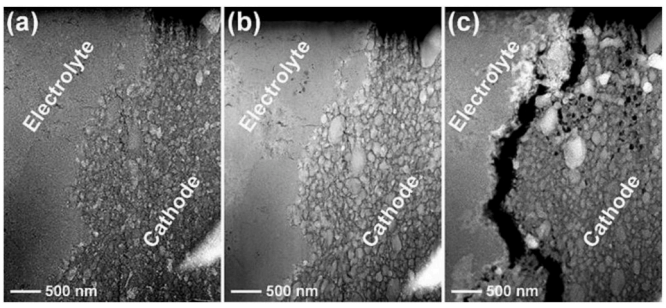

Fig. 3. STEM images of the electrolyte-cathode interface (a) as-prepared, (b) after the 1st cycle, (c) after the 2nd charging.

3.4. STEM-EDX analysis

The STEM-EDX map of a cross-section of an as-prepared cathode-electrolyte interface is shown in Fig. S4 (Supplementary Data). Even though the cathode consists of 90 wt% copper and 10 wt% carbon black, the oxygen map reveals significant amounts of oxygen in the cathode, which anti-correlates with the copper concentration. The origin of oxygen in the cathode materials is attributed to the carbon black, whereas the copper particles do not show significant oxidation. Small amounts of oxygen can also be observed in the electrolyte, which is more stable against oxidation. The La, Ba, and F maps reveal the good homogeneity of the electrolyte. The STEM-EDX map of the cathode-electrolyte interface after failure is shown in Fig. 5. The migration of fluorine into the Cu/C cathode can be observed from the fluorine distribution. Moreover, the diffusion of Cu into the electrolyte can also be seen. The strong volumetric change accompanying the Cu/CuF_2 reaction [26] probably led to Cu diffusion into the pores of the electrolyte to compensate for the volume change.

From the thick part of the sample right next to the area investigated *in situ*, a fresh thin area was prepared at the cathode-electrolyte interface after cycling to investigate potential thickness effects during *in situ* cycling. The morphological changes observed in this thick part and the thin area investigated *in situ* are comparable, confirming that the sample thickness does not significantly influence the morphological changes observed *in situ* even though surface effects might change the fluoride ion conductivity. A STEM-EDX map from this area is shown in Fig. 6. The fluoride migration into the Cu/C cathode can be seen more clearly compared to the initially thinned area. HRTEM imaging further confirmed the formation of CuF_2. Similar to the thin part, diffusion of Cu into the electrolyte was also observed in the thick part of the sample, presumably due to the effects of the volumetric changes associated with the fluorination [47]. In addition, the formation of Cu oxide may lead to an inhomogeneous distribution of the current density through the cathode and hence, a localized overheating that favors void formation. Moreover, the molybdenum map reveals Mo enrichment at the electrolyte-electrode interface, which could be a failure mode due to impurities.

3.5. TEM and HRTEM study

BF-TEM imaging is used to determine the particle size in the Cu/C cathode and to investigate the cathode-electrolyte interface before cycling (Fig. S5a, Supplementary Data). The TEM images reveal that the Cu/C cathode material consists of nano-particles 40–250 nm in size while the electrolyte consists of denser and smaller nano-particles. The small particle size and fine mixture of the electrode materials are essential for the electrochemical performance of the cell as a high contact area and good ion and electron diffusion pathways are required for a fast and complete conversion reaction [48–50]. HRTEM micrographs have been used to characterize the crystal structure of the cathode materials. Fig. S5b in the Supplementary Data shows a HRTEM micrograph and the corresponding Fast Fourier Transform (FFT) of cathode material of the as-prepared cell. The HRTEM micrograph confirms the high crystallinity of the cathode and the presence of Cu. The lattice spacings of a Cu particle measured from the FFT are in good agreement with the tetragonal phase of copper metal ($a = b = 2.892$ Å, $c = 2.708$ Å, $\alpha = \beta = \gamma = 90.0$) [ICSD-248435].

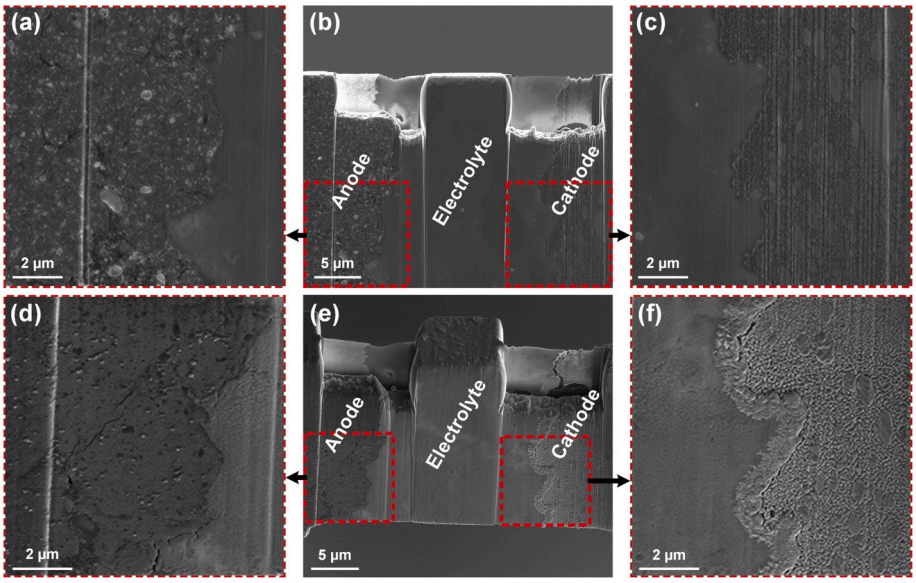

Fig. 4. SEM images of (a) thick area at anode-electrolyte before cycling, (b) full cell before cycling, (c) thick area of the electrolyte-cathode interface before cycling, (d) thick area of the anode-electrolyte after cycling, (e) full cell after cycling, (f) thick area of the electrolyte-cathode interface after cycling.

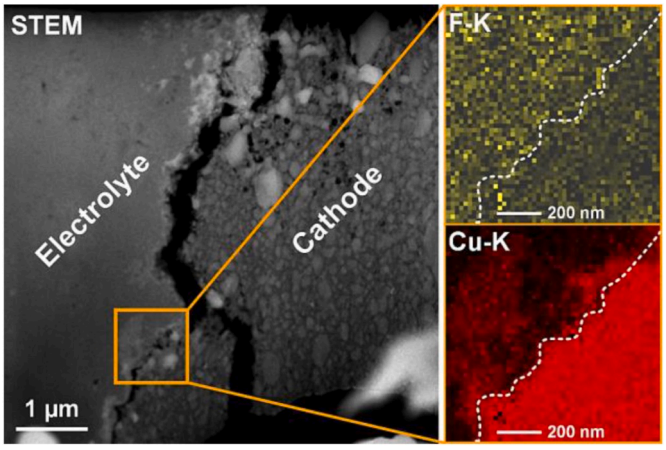

Fig. 5. STEM-EDX map of the cathode-electrolyte interface after failure.

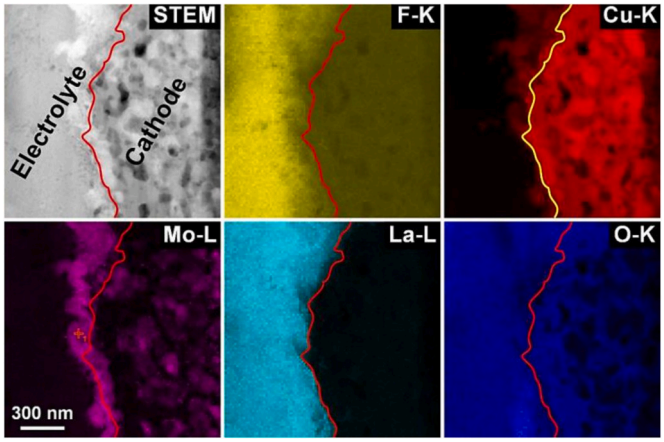

Fig. 6. STEM-EDX map of the new thinned area of the cathode-electrolyte interface.

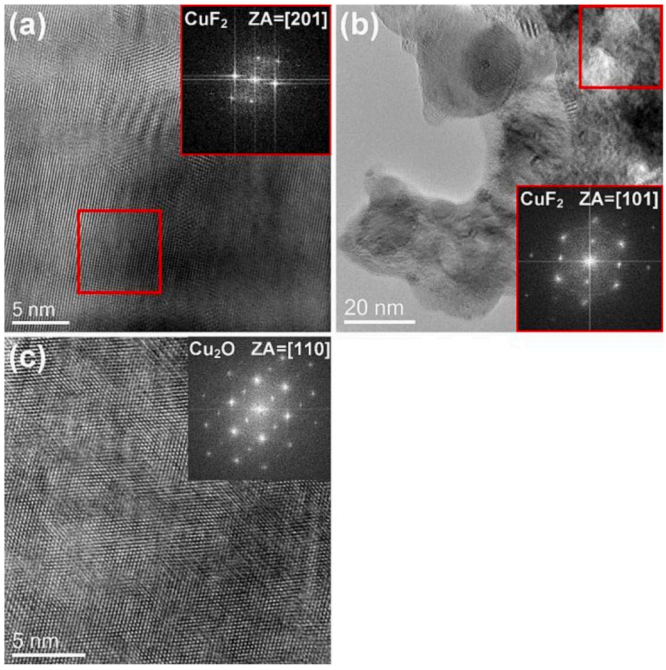

Fig. 7. HRTEM of the cathode after cycling and the corresponding FFTs. The image (a) has been filtered using the HRTEM-filter script (D. R. G. Mitchell, v2.0, Jan 14).

TEM and HRTEM micrographs of the Cu/C cathode after failure and the corresponding FFTs are shown in Fig. 7a, b, c, confirming the presence of CuF_2 after cycling. The measured lattice spacings fit well to the monoclinic phase of copper (II) fluoride (a = 3.309 Å, b = 4.569 Å, c = 5.362 Å, α = 90.0, β = 121.11, γ = 90.0) [ICSD-9788]. In addition to CuF_2 formation, the presence of Cu_2O is confirmed by HRTEM as was expected from the CV peak at around 2 V. The lattice spacings of the Cu_2O crystal are in good agreement with cubic copper (I) oxide (a = b = c = 4.27 Å, α = β = γ = 90.0) [ICSD-173982]. Furthermore, BF-TEM images of the cathode-electrolyte interface after failure are shown in Fig. 8a, b, c. The images reveal the formation of spherical-particles at the interface (Fig. 8a) in addition to amorphous carbon (Fig. 8c). The

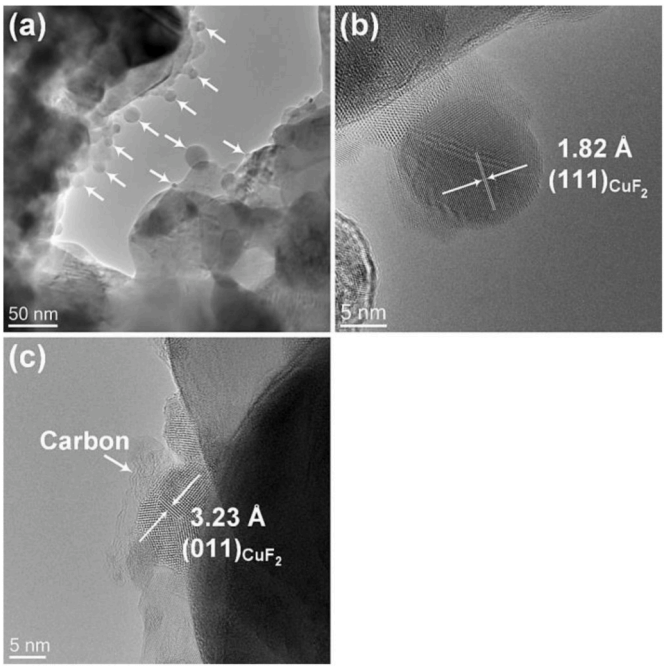

Fig. 8. TEM and HRTEM images of the cathode-electrolyte interface after failure.

formation of voids and spherical-particles would fit the hypothesis that the localized overheating has occurred due to an inhomogeneous current density in the cathode, as a result of Cu oxide and fluoride formation and their inhomogeneous distribution within the conductive matrix. These spherical-particles were confirmed by HRTEM to be copper (II) fluoride, (Fig. 8b).

4. Conclusion

Electrochemical cycling of a secondary fluoride ion cell (Cu + C// $La_{0.9}Ba_{0.1}F_{2.9}$//MgF_2+Mg + $La_{0.9}Ba_{0.1}F_{2.9}$+C) has been performed *in situ* inside a TEM. The CV peaks measured during the *in situ* studies occurred at voltages comparable to *ex situ* TEM studies. The structural and morphological studies of the cathode after cycling showed the fluoride migration into the cathode composite forming copper (II) fluoride. However, in addition, copper (I) oxide was formed during charging, which might have caused localized overheating and, hence, the formation of voids and spherical-particles. The micron-sized cell fractured at the cathode-electrolyte interface during the 2^{nd} *in situ* charging as a result of the volumetric changes associated with the CuF_2 formation and limited free volume available to compensate the volume changes. Cracks and voids formation were observed both in the thin and thick part of the sample thus confirming that these effects are not just due to the thin film setup for *in situ* TEM. Moreover, Cu diffusion from the composite cathode into the electrolyte was observed, presumably associated with the volumetric changes and some porosity of the electrolyte.

In summary, reliable *in situ* TEM analysis is possible for all-solid-state fluoride ion battery systems with a setup closely resembling bulk solid-state cells. However, the development of a good fluoride electrolyte with high ionic conductivity at RT, preventing oxidation of the electrode materials, and optimizing the porosity and pore size distribution of the electrodes and electrolyte are essential to enhance the performance of the fluoride ion battery to meet the requirements for the new applications.

CRediT authorship contribution statement

Mohammed Hammad Fawey: Writing - original draft, Methodology, Formal analysis, Investigation, Visualization, Writing - review & editing. **Venkata Sai Kiran Chakravadhanula:** Formal analysis, Investigation, Writing - review & editing. **Anji Reddy Munnangi:** Resources, Investigation. **Carine Rongeat:** Resources, Investigation. **Horst Hahn:** Writing - review & editing, Supervision. **Maximilian Fichtner:** Investigation, Funding acquisition. **Christian Kübel:** Conceptualization, Project administration, Formal analysis, Investigation, Writing - review & editing, Funding acquisition.

Acknowledgment

The authors acknowledge financial support from the European Union's Seventh Programme for research, technological development and demonstration under grant agreement No. 608575 (Hi-C) and from the DFG through the research unit FOR2093, as well as the support of the Karlsruhe Nano Micro Facility (KNMF) for access to the Electron Microscopy and Spectroscopy facilities. M. H. Fawey acknowledges a PhD scholarship of the IDB. The authors acknowledge support by Julia Ivanisenko for compressing the battery pellets. This work contributes to the research performed at CELEST (Center for Electrochemical Energy Storage Ulm-Karlsruhe).

Appendix A. Supplementary data

Supplementary data to this article can be found online at https://doi.org/10.1016/j.jpowsour.2020.228283.

References

[1] J. Jaguemont, L. Boulon, Y. Dubé, A comprehensive review of lithium-ion batteries used in hybrid and electric vehicles at cold temperatures, Appl. Energy 164 (2016) 99–114, https://doi.org/10.1016/j.apenergy.2015.11.034.
[2] A.J. Crawford, Q. Huang, M.C.W. Kintner-Meyer, J.-G. Zhang, D.M. Reed, V. L. Sprenkle, V.V. Viswanathan, D. Choi, Lifecycle comparison of selected Li-ion battery chemistries under grid and electric vehicle duty cycle combinations, J. Power Sources 380 (2018) 185–193, https://doi.org/10.1016/j.jpowsour.2018.01.080.
[3] A.-I. Stan, M. Swierczynski, D.-I. Stroe, R. Teodorescu, S.J. Andreasen, K. Moth, A comparative study of lithium ion to lead acid batteries for use in UPS applications, in: Telecommunications Energy Conference (INTELEC), 2014 IEEE 36th International, IEEE, 2014, pp. 1–8, https://doi.org/10.1109/INTLEC.2014.6972152.
[4] G. Pistoia, Applications – PORTABLE | portable devices: batteries, in: Encyclopedia of Electrochemical Power Sources, Elsevier, 2009, pp. 29–38, https://doi.org/10.1016/B978-044452745-5.00358-0.
[5] D. Zhou, L. Xue, L. Wang, N. Wang, W.-M. Lau, X. Cao, Self-chargeable sodium-ion battery for soft electronics, Nanomater. Energy 61 (2019) 435–441, https://doi.org/10.1016/j.nanoen.2019.04.068.
[6] W.Q. Walker, Rechargeable lithium batteries for aerospace applications, in: Rechargeable Lithium Batteries, Elsevier, 2015, pp. 369–383, https://doi.org/10.1016/B978-1-78242-090-3.00014-6.
[7] M.E. Sotomayor, C. de la Torre-Gamarra, B. Levenfeld, J.-Y. Sanchez, A. Varez, G.-T. Kim, A. Varzi, S. Passerini, Ultra-thick battery electrodes for high gravimetric and volumetric energy density Li-ion batteries, J. Power Sources 437 (2019) 226923, https://doi.org/10.1016/j.jpowsour.2019.226923.
[8] J. Shin, T.-H. Kim, Y. Lee, E. Cho, Key functional groups defining the formation of Si anode solid-electrolyte interphase towards high energy density Li-ion batteries, Energy Storage Materials 25 (2020) 764–781, https://doi.org/10.1016/j.ensm.2019.09.009.
[9] e.V. Forschungsstelle für Energiewirtschaft, e. v. FFE, Range Assessment of Current Lithium Reserves, n.d. https://www.ffe.de/en/topics-and-methods/resources-and-climate-protection/666-range-assessment-of-current-lithium-reserves.
[10] M.M. Thackeray, C. Wolverton, E.D. Isaacs, Electrical energy storage for transportation—approaching the limits of, and going beyond, lithium-ion batteries, Energy Environ. Sci. 5 (2012) 7854, https://doi.org/10.1039/c2ee21892e.
[11] J.B. Goodenough, Y. Kim, Challenges for rechargeable batteries, J. Power Sources 196 (2011) 6688–6694, https://doi.org/10.1016/j.jpowsour.2010.11.074.
[12] C. Chen, T. Yu, M. Yang, X. Zhao, X. Shen, An all-solid-state rechargeable chloride ion battery, Advanced Science 6 (2019) 1802130, https://doi.org/10.1002/advs.201802130.
[13] X. Zhao, S. Ren, M. Bruns, M. Fichtner, Chloride ion battery: a new member in the rechargeable battery family, J. Power Sources 245 (2014) 706–711, https://doi.org/10.1016/j.jpowsour.2013.07.001.

[14] M. Anji Reddy, M. Fichtner, Batteries based on fluoride shuttle, J. Mater. Chem. 21 (2011) 17059, https://doi.org/10.1039/c1jm13535j.

[15] M. Hammad Fawey, V.S.K. Chakravadhanula, M.A. Reddy, C. Rongeat, T. Scherer, H. Hahn, M. Fichtner, C. Kübel, In situ TEM studies of micron-sized all-solid-state fluoride ion batteries: preparation, prospects, and challenges, Microsc. Res. Tech. 79 (2016) 615–624, https://doi.org/10.1002/jemt.22675.

[16] H. Bhatia, D.T. Thieu, A.H. Pohl, V.S.K. Chakravadhanula, M.H. Fawey, C. Kübel, M. Fichtner, Conductivity optimization of tysonite-type $La_{1-x}Ba_xF_{3-x}$ solid electrolytes for advanced fluoride ion battery, ACS Appl. Mater. Interfaces 9 (2017) 23707–23715, https://doi.org/10.1021/acsami.7b04936.

[17] K. Mori, A. Mineshige, T. Saito, M. Sugiura, Y. Ishikawa, F. Fujisaki, K. Namba, T. Kamiyama, T. Otomo, T. Abe, T. Fukunaga, Experimental visualization of interstitialcy diffusion pathways in fast-fluoride-ion-conducting solid electrolyte $Ba_{0.6}La_{0.4}F_{2.4}$, ACS Appl. Energy Mater. 3 (2020) 2873–2880, https://doi.org/10.1021/acsaem.9b02494.

[18] J. Haruyama, K. Okazaki, Y. Morita, H. Nakamoto, E. Matsubara, T. Ikeshoji, M. Otani, Two-phase reaction mechanism for fluorination and defluorination in fluoride-shuttle batteries: a first-principles study, ACS Appl. Mater. Interfaces 12 (2020) 428–435, https://doi.org/10.1021/acsami.9b13978.

[19] J. Song, J. She, D. Chen, F. Pan, Latest research advances on magnesium and magnesium alloys worldwide, Journal of Magnesium and Alloys 8 (2020) 1–41, https://doi.org/10.1016/j.jma.2020.02.003.

[20] R. Deivanayagam, B.J. Ingram, R. Shahbazian-Yassar, Progress in development of electrolytes for magnesium batteries, Energy Storage Materials 21 (2019) 136–153, https://doi.org/10.1016/j.ensm.2019.05.028.

[21] J. Li, T. Risthaus, J. Wang, D. Zhou, X. He, N. Ehteshami, V. Murzin, A. Friesen, H. Liu, X. Hou, M. Diehl, E. Paillard, M. Winter, J. Li, The effect of Sn substitution on the structure and oxygen activity of $Na_{0.67}Ni_{0.33}Mn_{0.67}O_2$ cathode materials for sodium ion batteries, J. Power Sources 449 (2020) 227554, https://doi.org/10.1016/j.jpowsour.2019.227554.

[22] C. Luo, J.J. Shea, J. Huang, A carboxylate group-based organic anode for sustainable and stable sodium ion batteries, J. Power Sources 453 (2020) 227904, https://doi.org/10.1016/j.jpowsour.2020.227904.

[23] L. Zheng, R. Fielden, J.C. Bennett, M.N. Obrovac, Hexagonal and monoclinic $NaNi_{0.8}Co_{0.15}Al_{0.05}O_2$ (Na-NCA) for sodium ion batteries, J. Power Sources 433 (2019) 226698, https://doi.org/10.1016/j.jpowsour.2019.226698.

[24] C. Rongeat, M.A. Reddy, R. Witter, M. Fichtner, Nanostructured fluorite-type fluorides as electrolyte for fluoride ion batteries, J. Phys. Chem. C 117 (2013) 4943–4950, https://doi.org/10.1021/jp3117825.

[25] D.T. Thieu, M.H. Fawey, H. Bhatia, T. Diemant, V.S.K. Chakravadhanula, R. J. Behm, C. Kübel, M. Fichtner, CuF_2 as reversible cathode for fluoride ion batteries, Adv. Funct. Mater. 27 (2017) 1–11, https://doi.org/10.1002/adfm.201701051.

[26] C. Rongeat, M. Anji Reddy, T. Diemant, R.J. Behm, M. Fichtner, Development of new anode composite materials for fluoride ion batteries, J. Mater. Chem. 2 (2014) 20861–20872, https://doi.org/10.1039/C4TA02840F.

[27] C. Villevieille, Electrochemical characterization of rechargeable lithium batteries, in: Rechargeable Lithium Batteries, Elsevier, 2015, pp. 183–232, https://doi.org/10.1016/B978-1-78242-090-3.00007-9.

[28] M. Rosso, C. Brissot, A. Teyssot, M. Dollé, L. Sannier, J.-M. Tarascon, R. Bouchet, S. Lascaud, Dendrite short-circuit and fuse effect on Li/polymer/Li cells, Electrochim. Acta 51 (2006) 5334–5340, https://doi.org/10.1016/j.electacta.2006.02.004.

[29] Y. Feng, T.-D.-T. Ngo, M. Panagopoulou, A. Cheriet, B.M. Koo, C. Henry-de-Villeneuve, M. Rosso, F. Ozanam, Lithiation of pure and methylated amorphous silicon: monitoring by operando optical microscopy and ex situ atomic force microscopy, Electrochim. Acta 302 (2019) 249–258, https://doi.org/10.1016/j.electacta.2019.02.016.

[30] D. Chen, S. Indris, M. Schulz, B. Gamer, R. Mönig, In situ scanning electron microscopy on lithium-ion battery electrodes using an ionic liquid, J. Power Sources 196 (2011) 6382–6387, https://doi.org/10.1016/j.jpowsour.2011.04.009.

[31] R. Tao, J. Zhu, Y. Zhang, W.-L. Song, H. Chen, D. Fang, Quantifying the 2D anisotropic displacement and strain fields in graphite-based electrode via in situ scanning electron microscopy and digital image correlation, Extreme Mechanics Letters 35 (2020) 100635, https://doi.org/10.1016/j.eml.2020.100635.

[32] Y. Ding, T. Han, H. Zhang, M. Cheng, Y. Wu, X. Chen, M. Chi, J. Niu, J. Liu, A hollow Co_2SiO_4 nanosheet Li-ion battery anode with high electrochemical performance and its dynamic lithiation/delithiation using in situ transmission electron microscopy technology, Appl. Surf. Sci. 490 (2019) 510–515, https://doi.org/10.1016/j.apsusc.2019.06.088.

[33] J. Woods, N. Bhattarai, P. Chapagain, Y. Yang, S. Neupane, In situ transmission electron microscopy observations of rechargeable lithium ion batteries, Nanomater. Energy 56 (2019) 619–640, https://doi.org/10.1016/j.nanoen.2018.11.087.

[34] V. Vanpeene, A. King, E. Maire, L. Roué, In situ characterization of Si-based anodes by coupling synchrotron X-ray tomography and diffraction, Nanomater. Energy 56 (2019) 799–812, https://doi.org/10.1016/j.nanoen.2018.11.079.

[35] T.D. Hatchard, J.R. Dahn, In situ XRD and electrochemical study of the reaction of lithium with amorphous silicon, J. Electrochem. Soc. 151 (2004) A838, https://doi.org/10.1149/1.1739217.

[36] C. von Lüders, V. Zinth, S.V. Erhard, P.J. Osswald, M. Hofmann, R. Gilles, A. Jossen, Lithium plating in lithium-ion batteries investigated by voltage relaxation and in situ neutron diffraction, J. Power Sources 342 (2017) 17–23, https://doi.org/10.1016/j.jpowsour.2016.12.032.

[37] V. Zinth, C. von Lüders, J. Wilhelm, S.V. Erhard, M. Hofmann, S. Seidlmayer, J. Rebelo-Kornmeier, W. Gan, A. Jossen, R. Gilles, Inhomogeneity and relaxation phenomena in the graphite anode of a lithium-ion battery probed by in situ neutron diffraction, J. Power Sources 361 (2017) 54–60, https://doi.org/10.1016/j.jpowsour.2017.06.060.

[38] T. Yamanaka, T. Abe, K. Nishio, Z. Ogumi, In situ observation of fluoride shuttle battery reactions with dissolution-deposition mechanisms by Raman microscopy, J. Electrochem. Soc. 166 (2019) A635–A640, https://doi.org/10.1149/2.0931904jes.

[39] Z. Wei, A. Salehi, G. Lin, J. Hu, X. Jin, E. Agar, F. Liu, Probing Li-ion concentration in an operating lithium ion battery using in situ Raman spectroscopy, J. Power Sources 449 (2020) 227361, https://doi.org/10.1016/j.jpowsour.2019.227361.

[40] F. Badway, A.N. Mansour, N. Pereira, J.F. Al-Sharab, F. Cosandey, I. Plitz, G. G. Amatucci, Structure and electrochemistry of copper fluoride nanocomposites utilizing mixed conducting matrices, Chem. Mater. 19 (2007) 4129–4141, https://doi.org/10.1021/cm070421g.

[41] W. Baukal, Über reaktionsmöglichkeiten in elektroden von festkörperbatterien, Electrochim. Acta 19 (1974) 687–694, https://doi.org/10.1016/0013-4686(74)80011-3.

[42] T. Kozlova, In Situ Transmission Electron Microscopy Investigations of Electromigration in Metals, Delft University of Technology, 2015, https://doi.org/10.4233/uuid:10b2fb31-9352-4527-a0dd-7bded605196b.

[43] I. Mohammad, R. Witter, Testing Mg as an anode against BiF_3 and SnF_2 cathodes for room temperature rechargeable fluoride ion batteries, Mater. Lett. 244 (2019) 159–162, https://doi.org/10.1016/j.matlet.2019.02.052.

[44] F. Gschwind, J. Bastien, Parametric investigation of room-temperature fluoride-ion batteries: assessment of electrolytes, Mg-based anodes, and BiF_3-cathodes, J. Mater. Chem. A 3 (2015) 5628–5634, https://doi.org/10.1039/C4TA06625A.

[45] K. Aarstad, G. Tranell, G. Pettersen, T.A. Engh, Various techniques to study the surface of magnesium protected by SF_6, Magnesium Technology (2003) 5–10, 2003.

[46] F. Gschwind, G. Rodriguez-Garcia, D.J.S. Sandbeck, A. Gross, M. Weil, M. Fichtner, N. Hörmann, Fluoride ion batteries: theoretical performance, safety, toxicity, and a combinatorial screening of new electrodes, J. Fluor. Chem. 182 (2016) 76–90, https://doi.org/10.1016/j.jfluchem.2015.12.002.

[47] C. Julien, Z. Stoynov, Materials for Lithium-Ion Batteries, Springer Netherlands, Dordrecht, 2000, https://doi.org/10.1007/978-94-011-4333-2.

[48] T.V.S.L. Satyavani, B. Ramya Kiran, V. Rajesh Kumar, A. Srinivas Kumar, S. V. Naidu, Effect of particle size on dc conductivity, activation energy and diffusion coefficient of lithium iron phosphate in Li-ion cells, Engineering Science and Technology, Int. J. 19 (2016) 40–44, https://doi.org/10.1016/j.jestch.2015.05.011.

[49] E. Pohjalainen, T. Rauhala, M. Valkeapää, J. Kallioinen, T. Kallio, Effect of $Li_4Ti_5O_{12}$ particle size on the performance of lithium ion battery electrodes at high C-rates and low temperatures, J. Phys. Chem. C 119 (2015) 2277–2283, https://doi.org/10.1021/jp509428c.

[50] L.S.-K. Lee S-M, S.-T. Lee, D.-H. Lee, S.-H. Lee, S.-S. Han, Effect of particle size on the density and ionic conductivity of $Na_3Zr_2Si_2PO_{12}$ NASICON, J. Ceram. Process. Res. 16 (2015) 49–53.